# Ablation and nanostructuring of metals by femtosecond laser pulses

S.I. Ashitkov, P.S. Komarov, A.V. Ovchinnikov, E.V. Struleva,
V.V. Zhakhovskii, N.A. Inogamov, M.B. Agranat

***Abstract.*** **Using an interferometric continuous monitoring technique, we have investigated the motion of the surface of an aluminium target in the case of femtosecond laser ablation at picosecond time delays relative to the instant of laser exposure. Measurements of the temporal target dispersion dynamics, molecular dynamics simulation results and the morphology of the ablation crater have demonstrated a thermomechanical (spall) nature of the disruption of the condensed phase due to the cavitation-driven formation and growth of vapour phase nuclei upon melt expansion, followed by the formation of surface nanostructures upon melt solidification. The tensile strength of heated aluminium in a condensed state has been determined experimentally at an expansion rate of ~$10^9$ s$^{-1}$.**

*Keywords: femtosecond laser pulse, ablation, nanostructures.*

## 1. Introduction

Femtosecond laser systems are currently an important tool for basic research into nonequilibrium processes in condensed media and are widely used in modern precision laser processing technologies and for creating novel functional nanomaterials. In contrast to the evaporation process typically induced on the surface of metals and semiconductors by millisecond and nanosecond laser pulses, the main mechanism in the case of femtosecond pulses is thermomechanical ablation, which removes a surface nanolayer as a result of high tensile stress generation in the material [1]. Rapid isochoric heating and nonequilibrium bulk melting of a surface layer on a picosecond timescale are accompanied by the development of cavitation processes in the melt rarefaction wave and ablation of some melt in the form of a thin spall plate in a condensed state [2–7]. Subsequent rapid cooling and solidification of the residual melt lead to both the bulk modification of a surface nanolayer [8] and the formation of surface nanotopography [9, 10] with specific optical and thermophysical properties.

**S.I. Ashitkov, P.S. Komarov, A.V. Ovchinnikov, E.V. Struleva,**
**M.B. Agranat** Joint Institute for High Temperatures, Russian Academy of Sciences, Izhorskaya ul. 13/2, 125412 Moscow, Russia;
e-mail: ashitkov11@yandex.ru;
**V.V. Zhakhovskii** Dukhov All-Russia Research Institute of Automatics, Sushchevskaya ul. 22, 127055 Moscow, Russia;
e-mail: 6asilz@gmail.com;
**N.A. Inogamov** Landau Institute for Theoretical Physics, Russian Academy of Sciences, prosp. Akad. Semenova 1-A, 142432 Chernogolovka, Moscow region, Russia;
e-mail: nailinogamov@gmail.com

In this study, picosecond-resolution spectral interferometry with continuous motion tracking has been utilised to follow the femtosecond laser ablation of metals. Using aluminium as an example, we have demonstrated the possibility to determine the magnitude and spatial localisation of the stress that causes fracture of the metal in a condensed state during high-speed stretching. The surface nanomorphology of a metallic target around the ablation crater has been examined by scanning electron microscopy (SEM). We also present molecular dynamics simulation results for the ablation process in the metal, including the evolution of the cavitation ensemble of vapour phase bubbles, followed by the formation of nanofoam and surface nanostructuring upon nanofoam solidification.

In studies of hydrodynamic effects in picosecond laser ablation, the widest use is made of the pump–probe technique, which offers a time resolution as high as ~$10^{-13}$ s. In femtosecond interference microscopy, a widely used technique, the dynamics of the ablation process are examined via the multiple repetition of experiments at a varied time delay between heating and probe pulses [11–13]. This imposes significant limitations on the laser pulse stability and the uniformity of samples in properties.

Most state-of-the-art high-power femtosecond laser systems take advantage of the chirped pulse amplification (CPA) method. In connection with this, spectral interferometric techniques [14–16], in which a chirped pulse serves as a frequency-modulated probe pulse, have recently been used for the continuous tracking of the motion of surfaces on a picosecond timescale. The use of this approach enables continuous monitoring of single-shot process dynamics.

In shock wave experiments, the breaking tensile stress can be determined by measuring the free surface velocity profile $u(t)$ of a test specimen using VISAR or ORVIS interferometric laser Doppler velocimetry systems [17]. The time resolution of these instruments is limited to ~$10^{-9}$ s and is determined by the delay arms of their interferometers. In the picosecond range, use is made of interferometers for determining the displacement of the surface, $z(t)$, which is then differentiated to give the velocity profile $u(t)$ [15, 16].

## 2. Experimental

The optical layout used in our measurements is shown in Fig. 1. The femtosecond pulse source used was a Legend Ti:sapphire laser system (Coherent Inc.), which generated 40-fs pulses at a wavelength of 800 nm with a pulse energy of up to 2 mJ. A small part of an amplified chirped pulse was removed from the laser channel before the compressor and sent to a measurement system (displacement-measuring inter-
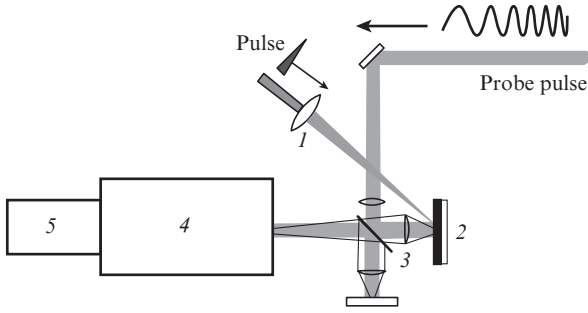
**Figure 1.** Schematic of the optical measurement system: (*1*) focusing lens, (*2*) target, (*3*) Michelson interferometer, (*4*) spectrometer, (*5*) CCD camera.

ferometer). The remainder was compressed to a femtosecond duration and then heated a target.

As test samples, we used 0.5-μm-thick aluminium and gold films grown on glass substrates.

The heating pulse energy $E$ was varied gradually using a polarisation attenuator composed of a half-wave plate and Glan prism and was measured with a photodiode. The photodiode was calibrated using a Sigma calorimeter (Coherent Inc.), which was introduced into the beam just before the target. The p-polarised heating radiation was focused onto the target at a 45° angle of incidence by a lens (*1*) with a focal length of 30 cm. The focusing system ensured a Gaussian spatial energy density distribution $F(x, y)$ across the focal spot on the target, with a 1/e characteristic radius $r_0 = 28$ μm. The parameters $r_0$ and $F_0$ of the Gaussian distribution across the focal spot were estimated using a procedure based on measurements of the ablation crater size as a function of laser pulse energy [18]. The procedure was also used to evaluate the ablation threshold $F_a$.

A sample (*2*) was placed on a computer-controlled three-axis micromanipulator, which ensured translation of the sample in three mutually perpendicular directions ($xyz$) in 1.25-μm steps. To perform each new measurement, the target was moved by 200 μm in the $xy$ plane. By moving the sample along the $z$ axis, it was positioned in the object plane of the micro-objective of the interferometer.

To follow the hydrodynamic motion of the ablation layer, we used a frequency-modulated (chirped) pulse about 300 ps in duration, with a centre wavelength $\lambda_0 = 795$ nm and a spectral bandwidth $\Delta\lambda = 40$ nm. To this end, part of the laser radiation after a regenerative amplifier was sent to a Michelson interferometer (*3*) by a partially transparent broadband mirror with a transmittance $T \approx 80\%$ through an optical delay line.

The optical delay line served to exactly match the arrival times of heating and probe pulses and to calibrate the time scale of our measurements [15]. The optical delay line consisted of broadband dielectric mirrors mounted on a computer-controlled motor-driven positioning system with a 2.5-μm displacement step and 300-mm base, which allowed the time delay $\Delta\tau$ between heating and probe pulses to be varied in the range 0–2 ns in 8-fs steps.

The absorption of a heating laser pulse in the surface layer of a target leads to motion of the surface of the sample. To measure the displacement of the surface as a function of time, $z(t)$, we used a Michelson interferometer, and an image of the sample surface was transferred to the entrance slit of a spectrometer (*4*) (Linnik configuration). The image was trans-

ferred in the sample arm of the interferometer with a magnification $\Gamma = 20^\times$ using a micro-objective with a numerical aperture NA = 0.2. The reference arm of the interferometer was formed by a similar objective and a dielectric mirror. The reference mirror of the interferometer was moved by a micropositioning system, which allowed us to equalise the optical lengths of the reference and sample arms. An equalisation criterion was that the interference fringes at the interferometer output had the highest contrast. The convergence angle of the interferometer beams was adjusted so that the interference fringes were perpendicular to the entrance slit of the spectrometer.

The frequency-modulated signal at the interferometer output was decomposed into a spectrum by an Acton-2300i Czerny–Turner grating spectrometer with a focal length of 300 mm. The beam arrived at the spectrometer through its entrance slit and was then decomposed into a spectrum (along the $x$-coordinate), which was recorded at the output by a CCD camera (*5*). In addition, the spatial distribution of the radiation incident on the slit was obtained along the $y$-coordinate. The flat focal surface in this configuration allowed us to obtain high resolution over the entire working spectral range.

The optical signals at the spectrometer output were recorded by a SensiCam QE cooled 12-bit CCD camera (PCO CCD Imaging) with a 1375×1375 pixel resolution.

The spectrometer used in the measurement system was equipped with a motor-driven turret head with a flat mirror and a diffraction grating ruled at 600 lines mm⁻¹. The spectrometer was able to both measure spectra and transfer an entrance slit image. This measurement configuration ensures continuous monitoring of the process dynamics with a time resolution $\delta t \approx 1$ ps in the time interval $\Delta\tau = 0 - 230$ ps.

The use of Fourier analysis of two-dimensional interferograms allows one to accurately restore the phase change of the reflected probe wave, which enables the displacement of the surface to be measured with an accuracy of a few nanometres. The algorithm of such measurements is to compare phase images before an experiment and during the motion of the target surface. In each experiment, three interferograms are obtained: an interferogram of the sample surface before a heating pulse (initial), an interferogram of the surface at the instant when a shock wave emerges (temporal) and an interferogram after the process is completed, about several seconds after the exposure (final).

Comparison of the $\Delta\varphi_{in}(y, t)$ and $\Delta\varphi_{tr}(y, t)$ phase distributions obtained by Fourier analysis of the initial and temporal interferograms provides information about the phase change $\Delta\varphi_{ind}(y, t)$ induced by surface motion:

$$\Delta\varphi_{ind}(y, t) = \Delta\varphi_{tr}(y, t) - \Delta\varphi_{in}(y, t). \qquad (1)$$

Similarly, comparison of the initial and final phase distributions [$\Delta\varphi_{fin}(y)$] provides information about the residual deformation produced on the sample surface after the process, e.g. about the ablation crater morphology.

The displacement of the surface, $\Delta z$, is related to the phase change by

$$\Delta z(y, t) = \lambda(t)\Delta\varphi_{ind}(y, t)/4\pi. \qquad (2)$$

The uncertainty in phase measurements in the configuration in question, $\delta\varphi_{ind} \approx \pi/200$, corresponds to an uncertainty in the displacement of the surface $\delta z \approx \pm 1$ nm. Here $\delta\varphi_{ind}$ is

determined by phase fluctuations in the undisturbed part of the $\Delta\varphi_{ind}(y,t)$ phase distribution.

## 3. Results and discussion

Figure 2 shows the spatio-temporal phase change distribution $\Delta\varphi_{ind}(y,t)$ for a probe pulse, which illustrates the dynamics of the motion of the ablation layer of an aluminium target under the action of a heating pulse of 40 fs duration.
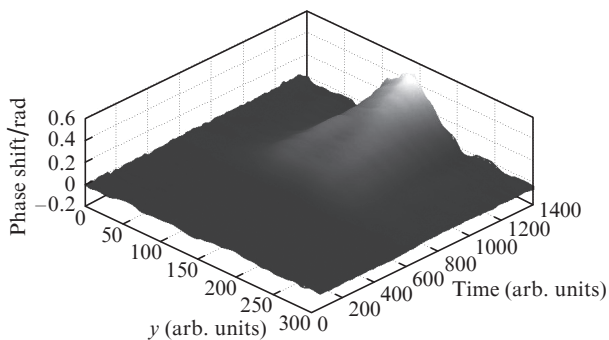


**Figure 2.** Spatio-temporal phase distribution $\Delta\varphi_{ind}(y,t)$ for a probe pulse, illustrating a spatially inhomogeneous motion of a surface aluminium layer during ablation by a 40-fs laser pulse with a Gaussian spatial distribution at an energy density $F_0/F_a = 1.2$.

Figure 3 shows surface displacement $z(t)$ and velocity $u(t)$ profiles as functions of time. The $z(t)$ profile was obtained for the central part of the affected zone by integrating over a spatial interval of $\pm 3$ μm, corresponding to an incident energy density range $\Delta F/F_0 = 0.05$. The velocity profile $u(t)$ was obtained by differentiating the $z(t)$ profile.
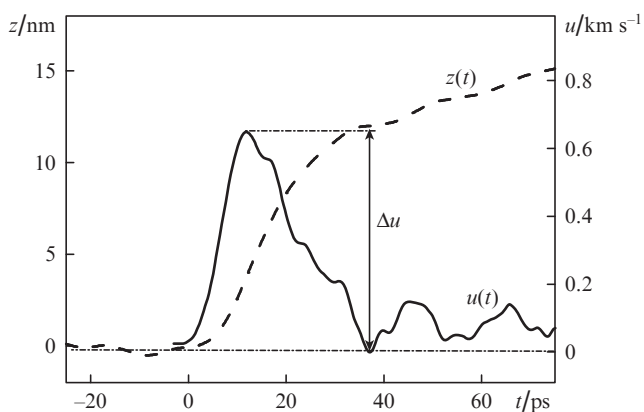


**Figure 3.** Time dependences of surface displacement $z(t)$ and velocity $u(t)$ for an aluminium test sample heated by a 40-fs laser pulse at an energy density $F_0/F_a = 1.2$.

The velocity profile $u(t)$ can be divided into three distinct portions. The maximum surface velocity $u_{max} \approx 0.65$ km s$^{-1}$ in the initial stage of acceleration is reached after about 10 ps of motion. The rapid acceleration during this time span is due to the pressure gradient $\partial p/\partial z$ in the heated layer of thickness $d_T$ and is the consequence of the isochoric nature of the heating process. The heating time of the ionic subsystem is determined by the electron–phonon heat transfer coefficient and is

2–3 ps in aluminium [19]. Unloading takes sonic times, $t_s \approx d_T/2c_0$, where $c_0$ is the sound velocity. Taking $c_0 = 5$ km s$^{-1}$ and $t_s \approx 10$ ps, we obtain an estimated thermal wave path length $d_T \approx 100$ nm, in good agreement with $d_T$ calculated for aluminium [19]. The observed decrease in the velocity of the boundary in the slowing down stage during the time interval 10–40 ps is caused by the resistance of the material to the tensile stress arising during its motion. At heating temperatures typical of ablation processes, 2–3 kK, nonequilibrium homogeneous melting takes $10^{-12}$ to $10^{-11}$ s [20]. A tensile stress exceeding the strength of the condensed phase, $\sigma_{liq}$, causes nucleation, which then leads to a discontinuity (spall). Next, an inertial layer motion stage begins. In this stage, an inertial velocity $u_{fin}$ of the centre of mass of the spall layer sets in, with slight sonic oscillations of the detached layer. The magnitude of $u_{fin}$ depends on to what extent the radiation energy density $F_0$ exceeds the ablation threshold $F_a$, and increases with increasing $F$. Figure 3 demonstrates that, at $F_0/F_a = 1.2$, the inertial layer dispersion velocity for aluminium is $u_{fin} \approx 0.1$ km s$^{-1}$.

By analogy with spall strength measurements in shock wave experiments [13, 17], the tensile strength of the condensed phase, $\sigma_{liq}$, can be roughly estimated using the linear acoustic relation

$$\sigma_{liq} = \rho_{liq}c_{liq}\Delta u/2. \tag{3}$$

Here, $\Delta u$ is the velocity decrement in the slowing down stage; $\rho_{liq}$ is the melt density; and $c_{liq}$ is the sound velocity in the melt. According to earlier results [21], molten aluminium at $T = 2$ kK has $\rho_{liq} = 2.16$ g cm$^{-3}$ and $c_{liq} = 3.6$ km s$^{-1}$. It is also worth noting that, in a rather wide temperature range (1–3 kK), the $\rho_{liq}c_{liq}$ product for aluminium varies by less than 15%. Therefore, for the experimentally determined value $\Delta u = 0.65$ km s$^{-1}$ at $F_0/F_a = 1.2$, the tensile stress that leads to aluminium melt discontinuity is $\sigma_{liq} = 2.5 \pm 0.3$ GPa. This value agrees well with molecular dynamics simulation results obtained by Agranat et al. [22] for liquid aluminium: $\sigma_{liq} \approx 2$ GPa at $T = 2$ kK.

The melt expansion rate $\dot{\varepsilon} = \dot{V}/V$ estimated using the relation [13, 17]

$$\dot{\varepsilon} = \frac{\Delta u}{\Delta\tau}\frac{1}{2c_{liq}} \tag{4}$$

is $\dot{\varepsilon} \approx 4\times10^9$ s$^{-1}$. Here $\Delta\tau = t_{min} - t_{max}$, where $t_{max}$ is the time corresponding to the maximum velocity in the $u(t)$ curve in Fig. 3 and $t_{min}$ is the time corresponding to the first minimum in $u(t)$.

The $\dot{\varepsilon}$ value obtained is comparable to the strain rates observed in aluminium in experiments with ultrashort shock waves [13]. In this case, the spall on the backside of the sample occurs in a solid phase, whose strength is about three times that obtained in this study for molten aluminium.

The aluminium spall layer thickness $L_{spall}$ near the ablation threshold at $F_0/F_a = 1.2$ can be estimated from the temporal layer dispersion dynamics $u(t)$ represented in Fig. 3, using the relation [13, 17]

$$L_{spall} = c_{liq}\Delta\tau/2. \tag{5}$$

At $\Delta\tau = 25$ ps, we have $L_{spall} \approx 45$ nm. This $L_{spall}$ value exactly corresponds to the depth $h$ of the crater (Fig. 4) produced on the surface of an aluminium sample in the same experiment.
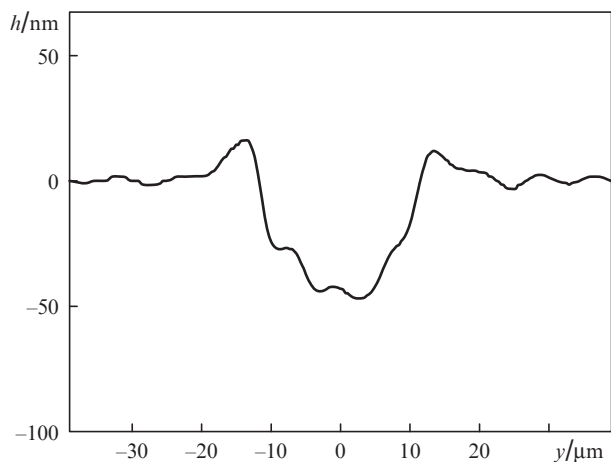
**Figure 4.** Ablation crater profile on aluminium at $F_0/F_a = 1.2$ obtained by Fourier analysis of the final interferogram.



**Figure 6.** SEM image of a part of the bottom of an ablation crater on the surface of a 500-nm-thick gold film sample after exposure to a 100-fs laser pulse with an energy density $F_0/F_a \approx 1.4$.

Figure 5 presents molecular dynamics simulation results on the expansion and cooling of a surface layer during femtosecond laser ablation of an aluminium film of thickness $L_x = 500$ nm. The simulation was performed at initial sample dimensions $L_x \times L_y \times L_z = 500 \times 240 \times 24$ nm for $172 \times 10^6$ atoms in a simulation box with periodic boundary conditions along the $y$ and $z$ axes. Computations were made for a ratio of the pulse energy density to ablation threshold $F_0/F_a \approx 1.4$. The electron thermal conductivity was taken into account in the computations by the Monte Carlo method.
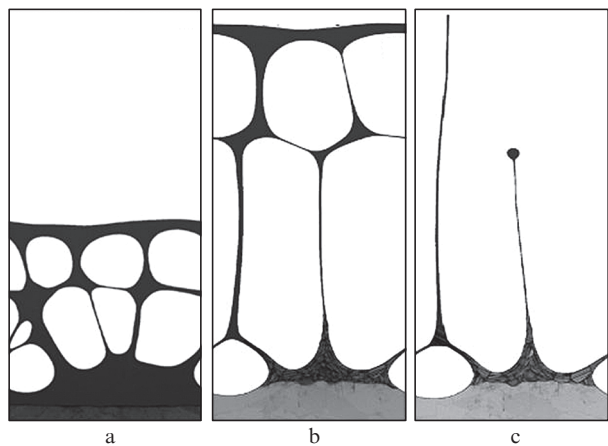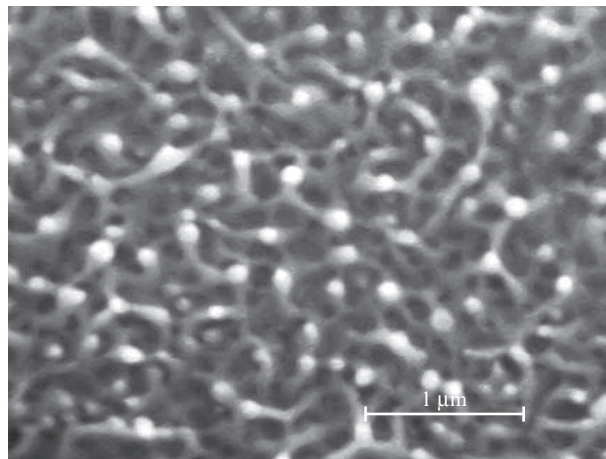
which leads to a drastic modification of the surface nanolayer after solidification.

Figure 6 is an SEM image of a part of the bottom of an ablation crater on the surface of a gold film sample after exposure to a femtosecond laser pulse.

It is seen that the surface morphology is represented by an array of branched filamentary nanostructures with spheres at their ends 70–150 nm in size, in qualitative agreement with molecular dynamics simulation results (Fig. 5).

## 4. Conclusions

The dynamics of the motion of the surface of a metallic target in the case of femtosecond laser ablation have been investigated using an interferometric method in a picosecond range, and the nanomorphology of the bottom of the ablation crater has been examined by SEM. We have presented molecular dynamics simulation results for the evolution of nanofoam during ablation layer expansion followed by surface nanostructuring after melt solidification. The simulation results fit well with SEM data on the nanomorphology of the bottom of the ablation crater. The present results indicate that the femtosecond laser ablation of metals has a thermomechanical spall nature and is due to the action of tensile stresses on a condensed phase. The strength of molten aluminium at an expansion rate of $4 \times 10^9$ s$^{-1}$ has been determined to be 2.5 GPa.



**Figure 5.** Surface layer structure evolution (a) 307, (b) 1024 and (c) 2202 ps after femtosecond laser ablation of aluminium. Transverse (horizontal) size of the simulation box is $L_y = 240$ nm.

It is seen in Fig. 5a that, in the picosecond range, active melt foaming occurs. Subsequently, the layer expands, leading to an increase in the size of nanocavities and a decrease in nanofoam membrane thickness (Fig. 5b). The next steps are the detachment of the top liquid layer, referred to as a spall plate, and membrane disruption, followed by the formation of surface nanotopography (Fig. 5c) as a result of the action of surface tension forces, melt cooling and solidification due to electron heat conduction. In Fig. 5, light grey colour corresponds to crystalline material. The melt cooling rate $\mathrm{d}T/\mathrm{d}t$ in the time interval under consideration is $10^{11}$ to $10^{12}$ K s$^{-1}$,

## References

1. Anisimov S.I., Luk'yanchuk B.S. *Usp. Fiz. Nauk*, **172**, 301 (2002).
2. Sokolowski-Tinten K., Bialkowski J., Cavalleri A., Von der Linde D., Oparin A., Meyer-ter-Vehn J., Anisimov S.I. *Phys. Rev. Lett.*, **81**, 224 (1998).
3. Ivanov D.S., Zhigilei L.V. *Phys. Rev. B*, **68**, 064114 (2003).
4. Bulgakova N.M., Stoian R., Rosenfeld A., Hertel I.V., Campbell E.B. *Phys. Rev. B*, **69**, 054102 (2004).

5. Agranat M.B., Anisimov S.I., Ashitkov S.I., Zhakhovskii V.V., Inogamov N.A., Nishihara K., Petrov Yu.V., Fortov V.E., Khokhlov V.A. *Appl. Surf. Sci.*, **253**, 6276 (2007).
6. Povarnitsyn M.E., Itina T.E., Sentis M., Khishchenko K.V., Levashov P.R. *Phys. Rev. B*, **75**, 235414 (2007).
7. Zhao X., Shin Y.C. *Appl. Surf. Sci.*, **283**, 94 (2013).
8. Ashitkov S.I., Inogamov N.A., Zhakhovskii V.V., Emirov Yu.N., Agranat M.B., Oleinik I.I., Anisimov S.I., Fortov V.E. *Pis'ma Zh. Eksp. Teor. Fiz.*, **95**, 192 (2012).
9. Vorobyev A.Y., Guo C. *Phys. Rev. B*, **72**, 195422 (2005).
10. Korolkov V.P., Ionin A.A., Kudryashov S.I., Seleznev L.V., Sinitsyn D.V., Samsonov R.V., Masliy A.I., Medvedev A.Zh., Goldenberg B.G. *Kvantovaya Elektron.*, **41**, 387 (2011) [*Quantum Electron.*, **41**, 387 (2011)].
11. Temnov V.V., Sokolovski-Tinten K., Zhou P., Von der Linde D. *J. Opt. Soc. Am. B*, **23**, 1954 (2006).
12. Gahagan K.T., Moore D.S., Funk D.J., Reho J.H., Rabie R.L. *J. Appl. Phys.*, **92**, 3679 (2002).
13. Ashitkov S.I., Agranat M.B., Kanel' G.I., Komarov P.S., Fortov V.E. *Pis'ma Zh. Eksp. Teor. Fiz.*, **92**, 568 (2010).
14. Crowhurst J.C., Armstrong M.R., Knight K.B., Zaug J.M., Behymer E.M. *Phys. Rev. Lett.*, **107**, 144302 (2011).
15. Whitley V.H., McGrane S.D., Eakins D.E., Bolme C.A., Moore D.S., Bingert J.F. *J. Appl. Phys.*, **109**, 013505 (2011).
16. Ashitkov S.I., Komarov P.S., Ovchinnikov A.V., Struleva E.V., Agranat M.B. *Kvantovaya Elektron.*, **43**, 242 (2013) [*Quantum Electron.*, **43**, 242 (2013)].
17. Eliezer S., Moshe E., Eliezer D. *Laser Part. Beams*, **20**, 87 (2002).
18. Liu M. *Opt. Lett.*, **7**, 196 (1982).
19. Anisimov S.I., Inogamov N.A., Petrov Y.V., Khokhlov V.A., Zhakhovskii V.V., Nishihara K., Agranat M.B., Ashitkov S.I., Komarov P.S. *Appl. Phys. A*, **92**, 797 (2008).
20. Rethfeld B., Sokolowski-Tinten K., Von der Linde D., Anisimov S.I. *Phys. Rev. B*, **65**, 092103 (2002).
21. Shock wave database: http://teos.ficp.ac.ru/rusbank/
22. Agranat M.B., Anisimov S.I., Ashitkov S.I., Zhakhovskii V.V., Inogamov N.A., Komarov P.S., Ovchinnikov A.V., Fortov V.E., Khokhlov V.A., Shelepin V.V. *Pis'ma Zh. Eksp. Teor. Fiz.*, **91**, 517 (2010).